DIAL Measurements of Free-Tropospheric Ozone Profiles in Huntsville, AL

Shi Kuang[1*], John Burris[2], Michael J. Newchurch[1], and Steve Johnson[3]

[1]University of Alabama in Huntsville, 320 Sparkman Dr., Huntsville, Alabama 35805, USA

[2]NASA-Goddard Space Flight Center, Code 694, Greenbelt, Maryland 20771, USA

[3]NASA-Mashall Space Flight Center, Office Code VP61, Huntsville, Alabama 35812, USA

**Corresponding author: kuang@nsstc.uah.edu*

ABSTRACT: A tropospheric ozone DIfferential Absorption Lidar (DIAL) system, developed jointly by NASA and the University of Alabama at Huntsville (UAH), measures free-tropospheric ozone profiles between 4-10 km. Located at 192 meters altitude in the Regional Atmospheric Profiling Laboratory for Discovery (RAPCD) on the UAH campus in Huntsville, AL, USA, this tropospheric ozone lidar operates under both daytime and nighttime conditions. Frequent coincident ozonesonde flights and theoretical calculations provide evidence to indicate the retrieval accuracy ranges from better than 8% at 4km to 40%-60% at 10 km with 750-m vertical resolution and 30-minute integration. With anticipated improvements to allow retrievals at both higher and lower altitudes, this ozone lidar, along with co-located aerosol and Doppler Wind Lidars, will provide a unique dataset for investigations of PBL and free-tropospheric chemical and dynamic processes.

1. Introduction

Measuring ozone variability at high spatial and temporal resolution increases our understanding of the Planetary Boundary Layer (PBL), PBL and free tropospheric exchange, stratosphere and troposphere exchange (STE), and the impact of lightning NOx on tropospheric ozone (*1*). Ozone, a triatomic oxygen molecule, is a key trace-gas species in the lower atmosphere. Within the troposphere, ozone is partially derived from transport processes that move ozone from the stratosphere into the troposphere and by the

oxidation of hydrocarbons originating from anthropogenic activity (*2*). Ozone's impact within the free-troposphere, which extends from the top of the PBL to a maximum altitude that varies between 9-16km depending on season and location, is more complex. Ozone is a powerful oxidant, and is harmful to both plant and animal life; it is a strong greenhouse gas and an important component of photochemical smog. However, it is also a key component of the atmospheric oxidizing cycle that cleans the air of harmful pollutants.

Several techniques currently exist for making range-resolved measurements of tropospheric ozone. The most common is the electrochemical concentration cell (ECC), which is attached to a balloon; ECCs have been used since the 1960's to monitor ozone. These ozonesondes can profile ozone with a 100m spatial resolution from the surface to 35km altitude with the accuracy of 5-10% (*3, 4*). Ozonesondes are attractive because of their low upfront cost and their well-characterized behavior. They are, however, not suitable for making continuous measurements because of cost and logistical considerations. Interesting atmospheric phenomena that vary over periods less than one day are particularly difficult to monitor using balloon sondes. Satellite observations can be used to derive total column ozone (*5*), stratospheric ozone (*6-11*), and to extend measurements to altitudes that are inaccessible to ozonesondes (*12*). More recently, high quality satellite observations of tropospheric ozone are becoming available (*4, 11, 13-18*). Although the satellite measurements can produce global maps of ozone, their current measurement uncertainties (*19, 20*) along with their coarse spatial and temporal resolution limit their ability to observe short-term variations of ozone. These techniques can be supplemented by lidar when a requirement exists for ozone retrievals with high temporal (from 1 min to several hours) and spatial resolution (from tens of meters to 2 km) over long periods. The DIAL technique minimizes the interference originating from aerosols and absorbing species such as SO_2, and eliminates the need for obtaining an absolute calibration of the instrument. DIAL has been successfully used to measure ozone within the planetary boundary layer (*21*), the free-troposphere (*22-27*), and the stratosphere (*28-31*) for several decades. DIAL is evolving from ground-based and airborne systems to systems suitable for long-term deployment in space (*32*). The technique derives ozone

50 concentrations by analyzing how rapidly the backscattered signals at two separate but closely spaced
51 wavelengths, one strongly absorbed by ozone and the other less strongly absorbed, fall off with altitude.
52 This measurement does not require that the absolute signal intensities are known but only how the two
53 signals change relative to one another with respect to altitude. The wavelengths are chosen to minimize
54 differential extinction due to aerosols, SO_2, and other species. The on-line to off-line signal ratio removes
55 the requirement that system parameters such as mirror size, pulse energy, and detection efficiency must be
56 known. Using electronically gated detection permits range-resolved measurements to a resolution as small
57 as ~15 m over acquisition times of several minutes. Although the up-front costs associated with a DIAL
58 system are considerably higher than a balloon ozonesonde operation, a DIAL system can acquire profiles
59 continuously under both daytime and nighttime conditions. The spatial and temporal resolution of a DIAL
60 lidar is more than sufficient to characterize short-term ozone variations for the photochemical studies of
61 vertical processes.

62 Several other research groups have employed ozone DIAL systems in both ground-based
63 configurations (*21, 24, 26, 31*) and aircraft configuration (*33, 34*) over the last two decades. The only
64 tropospheric ozone lidar in regular operation within the United States is located at the Jet Propulsion
65 Laboratory's Table Mountain facility northeast of Los Angeles in the San Gabriel Mountains (*35*). This
66 system Raman shifts 266 nm radiation to generate the on and offline wavelengths (289 and 299 nm). A lidar
67 system previously located on Fritz Peak in Colorado was operated for several years by Proffitt and Langford
68 (*26*). Like the McDermid system, the Proffitt lidar was located at relatively high altitude (~2300 m) to
69 maximize its altitude range and minimize interference from the boundary layer aerosols. Kempfer operated
70 a system in Germany using the output of a Raman shifted KrF excimer; this system was located at ~700 m
71 ASL (*36*). The location of the RAPCD ozone DIAL in the southeastern United States provides a unique
72 observational site within an interesting scientific area to study trace gas transport at the mid-latitudes (*37*).
73 Its low altitude facilitates the study of ozone within both polluted PBL and stratosphere-troposphere
74 exchange.

75 **2. System Description**

76 Housed in the RAPCD, the tropospheric ozone DIAL system is located on the UAH campus within the
77 Huntsville city limits at an elevation of 196 m ASL and is currently designed for operation within the
78 free-troposphere at altitudes between 4 and 10 km with a 150m vertical resolution. This approach permits
79 the determination of ozone number densities under both daytime and nighttime conditions at high precision.
80 Because of UAH's location, heavy aerosol pollution sometimes arises from sources such as forests,
81 agriculture, and a number of large, coal fired, power plants. Compared with the clean free-troposphere,
82 these aerosols require a larger dynamic range for detection system because of larger optical depth.
83 Moreover, the rapid change of aerosols (e.g. due to convective activity) increases the measurement
84 uncertainty for DIAL in the PBL and lower troposphere. Aside from aerosols, other differences between
85 stratospheric and tropospheric systems arise from the much larger dynamic range in signal strength
86 observed on tropospheric systems due to the signal's dependence on the $1/R^2$ term. The lower ozone
87 number densities observed in the troposphere require higher absorption per unit length to achieve the same
88 sensitivity as seen with stratospheric lidar systems. These differences have resulted in the Huntsville
89 system being configured somewhat differently from instruments designed to measure stratospheric ozone
90 or those that, while designed for tropospheric measurements, have been located at relatively high altitudes.

91 2.1 Wavelength selection

92 The optimum laser wavelengths result from the following four considerations: 1) The maximum
93 measurable altitude determines the shortest wavelength; 2) The ability to reduce solar radiation in daytime
94 operation determines the longest wavelength; 3) Minimizing the aerosol interference; 4) Avoiding SO_2
95 interference helps select among potential wavelength pairs. The DIAL wavelength selection is variable and
96 can be optimized for the local ozone distribution, the absorption arising from non-ozone species, the
97 measurement range and the specific system configuration including the output power, telescope mirror size
98 and the photomultiplier's (PMT's) dynamic range. The optimum ozone DIAL wavelength selection has
99 been explored by Megie (*38*) and further discussed by Proffitt (*26*) for tropospheric systems. We investigate

four specific criteria by model simulation under typically atmospheric conditions to select the optimum wavelength pair.

While large cross sections are desirable for measurement sensitivity, they cause enhanced signal attenuation due to both ozone absorption and Rayleigh extinction which limits the maximum altitude of the measurement and increases the signal acquisition time. Fig. 1 shows the 2005 mean ozone profile over Huntsville which is derived from the weekly ozonesonde measurements. The Huntsville ozone station at UAH routinely launches balloon ozonesondes weekly at 19:00 UTC on Saturday. The ozonesondes measure ozone up to 35 km with a 100m vertical resolution and 5-10% precision (*39*). These parameters are listed in Table 1. Fig. 2 presents the modeled signal returns from 270 to 300 nm with the configuration of a laser of 4 mJ/pulse, a telescope with 40 cm diameter, a PMT of 20% quantum efficiency, 5% totally optical transmission efficiency, 1976 U.S. standard atmosphere, the ozone profile in Fig.1, and a fall-winter rural aerosol model (*40*). The aerosol extinction profile was extrapolated to the 285-291 nm wavelength from original 550 nm assuming that the Angstrom exponent is equal 1.1 (*41*), which is an approximate value for rural-urban mixing aerosols. The dynamic range required for wavelengths below 270 nm to measure ozone between 4 and 10 km reaches or exceeds the maximum value of our PMT ($\sim 10^5$). The spring and summer tropospheric ozone concentrations in Huntsville are usually greater than the yearly average. Therefore, the potential on-line wavelength must be greater than 270 nm. Also, the wavelengths from 270 to 280 nm cannot provide sufficient signal-to-background ratio at 10 km due to the overloading limitation of our PMT. The background mainly consists of PMT dark counts and sky-light background. Dark counts are a function of the voltage and temperature of PMT (*42*) and are observed as about 200 photon/s for our experimental configuration. The comparison between modeled signals and background, as a function of wavelength, is shown in Fig. 3. The modeled signal is calculated using the same characteristics as Fig. 2. The expected sky background is simulated by NCAR TUV program (*43*) with the configuration in Table 1. The modeling indicates that the potential on-line wavelength pair for our configuration should be larger than 280 nm so that the detected signal is 1 order larger than the summation of sky background and dark

125 counts. To measure both wavelength channels by the same PMT and simplify the system design, we use a
126 broad band-pass filter (Barr Associates, 286.4/11nm), whose transmission as a function of wavelength is
127 shown by Fig. 4., to block the solar radiation. For a broadband band-pass filter the integrated sky
128 background over the filter bandwidth plus the dark counts actually determine the background for both
129 off-line and on-line wavelengths. The signal of the wavelengths below 285 is not large enough above 10 km
130 compared with the sum of sky background and dark counts to provide a useful measurement under mostly
131 atmospheric conditions. Increasing the laser power or removing neutral density filters could raise the
132 signal-to-background ratio at 10 km; however, this will lead to overloading of the PMTs at the near range.
133 The off-line wavelength is chosen at 291 because of both sky-background and interfering gases
134 considerations. The sky-background sharply increases in daytime with longer wavelength because of the
135 larger solar radiation even with an appropriate band-pass filter. As shown in Fig. 3, the signal at 291 nm is
136 about 2 orders of magnitude larger than sky background at 10 km. Fig. 5 [following Proffitt, *et al.*, 1997]
137 gives the signal-to-background ratio after passing through the band-pass filter. This model simulation
138 shows that the signal-to-background ratios are about 15 and 70 at 10 km for 285 and 291 respectively under
139 typical atmospheric condition, large enough to provide useful retrievals up to ~10 km.
140 Although retrieval errors due to aerosol interference are still of some concern in the PBL, they are
141 much less a concern in the free-troposphere. These errors can be explored by model simulation. Fig. 6
142 shows the modeled DIAL retrieval errors due to aerosol differential backscattering and extinction using the
143 parameters in Table 1 with a 750 m vertical resolution. The 285-291 pair will have a retrieval error at 4km
144 of less than 1% arising from uncorrected aerosol differential backscattering and extinction under typically
145 rural aerosol condition. If the aerosol loading is ten times higher, the error due to aerosol at 4 km increases
146 to 5%. These model simulations suggest that the errors due to aerosol above 4 km under both normal and
147 haze conditions are small relative to the statistical uncertainty which will be shown in later sections. The
148 error due to uncorrected Rayleigh extinction can be estimated with either the local sonde data or an
149 atmospheric model based on local climatology within the accuracy of 1% and will not be discussed here

150 further. Errors due to aerosol are extremely difficult to correct without additional local measurements
151 because of their large variability. These errors are sensitive to the wavelength pair and will increase with the
152 heavier aerosol loading. An approximate correction for aerosol has been given by Browell in 1985; at this
153 time, we make no aerosol correction in the free tropospheric lidar retrievals.

154 Constraining the daytime wavelengths below 292 nm requires that the impact of SO_2 is carefully
155 considered because its cross sections are comparable to those of ozone. The differential cross section of
156 SO_2 for 285-291 pair is $-4.8\times10^{-20}cm^2$ at 295 K (*44*). The error due to SO_2 is about -0.01% by assuming
157 that the SO_2 mixing ratio is 160 pptv under North America clean continental condition (*45*) and 60ppbv
158 ozone. This error could be up to -0.1% in a polluted air when SO_2 concentration reaches 1500 pptv.
159 However, its impact on our tropospheric measurements is negligible because it is much smaller than other
160 errors. Therefore, after fully considering the dynamic range of the PMTs, the measurement range, the
161 signal-to-background ratio, and the interfering species, we chose 285-291 wavelength pair for our lidar
162 system.

163 2.2 Hardware components

164 All DIAL systems consist of three major components: the transmitter, receiver, and detection
165 subsystems. The Huntsville transmitter consists of two identical dye lasers pumped by separate Nd:YAG
166 lasers. The characteristics of the DIAL system are listed in Table 2. Each pump laser has a fundamental
167 wavelength of 1064 nm, electro-optically Q-switched at 20 Hz using a plate polarizer, quarter waveplate,
168 and pockels cell. Each pulse is 5-7 ns Full Width at Half Maximum (FWHM) with a line-width of 1.0 cm^{-1}
169 and ~300 mJ of optical power. The output of each pump laser is frequency doubled by angle tuned
170 Potassium Dihydrogen Phosphate (KDP) crystals. The fundamental and frequency doubled pulses (532 nm)
171 are separated using dichroic mirrors (separators) where the fundamental is transmitted and absorbed by a
172 beam dump. The 532 nm pulses are reflected and redirected for use as a pump source for each tunable,
173 pulsed, dye laser as shown in Fig. 7. The dye lasers are software controlled with external computer systems
174 that select the user defined wavelength by rotating a reflection grating used to select a wavelength to be

amplified in the master oscillator. The dyes used as the gain medium are Rhodamine (R) 590 and 610. R590 is used to produce 570 nm output and a combination of both R590 and R610 is used to produce 582nm output. The output of each dye laser is frequency doubled using a Beta Barium Borate (BBO) crystal to produce pulses with energies of 3-5 mJ at 285 and 291nm and a divergence less than 1mrad. The divergences of both laser beams have been checked using a knife edge method (*46*). UV mirror configuration separates the UV pulses from their visible fundamentals while redirecting the UV pulses to a turning mirror which is aligned to reflect the pulses vertically into the atmosphere. Each laser pulse is externally triggered by a function generator #1 such that there is a 25 ms temporal separation between the firing of alternate pulses.

The receiver is a Newtonian telescope with a 40 cm primary and a two-channel aft optics unit as shown in Fig. 8. Its current location is in the RAPCD lidar laboratory (lat:34.7250, lon:-86.6450) where it views the atmosphere through a roof hatch with a 1m by 1m opening. A series of selectable apertures permit the telescope's field of view (FOV) to be changed as part of the alignment process. Provision exists to insert both band-pass and neutral density filters into the optical path to restrict the solar background and/or attenuate a channel's signal in the event that the returns are too high. The current band-pass filters have a transmission of 35% at 285 nm and $<10^{-8}$ beyond 300 nm as shown in Fig. 4. The system currently operates with two altitude channels. The signal is split, so the high-altitude channel receives ~90% of the light, and the low-altitude channel receives ~10%. This division effectively restricts the lower-altitude channel to no higher that ~4 km; the high-altitude channel routinely covers 4-10 km and on occasion has reached 12 km. The low-altitude system will be discussed in a separate paper. With the FOV of the receiver set at 1.5 mrad for normal operation, 0.9 m separation distance between the laser beam and the telescope axis, and 1mrad divergence of the laser beams, full overlap occurs at about 3 km. Larger FOVs lower the altitude at which full overlap between the laser and telescope occur but significantly increase background noise arising from the sun and city sky light.

RAPCD's detection system currently utilizes photon counting to facilitate operations at the maximum

200 achievable altitude. Two EMI 9813 QA PMTs, which have been used extensively for many years on a
201 number of Goddard Space Flight Center lidar systems, are used – one for each channel. The outgoing laser
202 pulse of each laser is detected by a photodiode (PD) laser-pulse detector, which sends the trigger to the
203 function generator #2. One channel of the function generator outputs a pulse to trigger a pulse generator that
204 controls the clock and bin width pulses for the return signal; the other channel sends a delayed pulse to gate
205 the PMT. The range bin width is set at 1 μs corresponding to an effective vertical resolution of 150 m. The
206 timing of the whole system including the laser trigger, gate signal, range bin width, clock, and ground bin
207 can be checked by an LED test (*47*) in which LED light simulates the backscattered return, and all signals
208 are monitored by an oscilloscope. The signal recording of the MCS board is supposed to start the same time
209 as the PD detection of laser-pulse trigger for our setting. But a small offset between them has been observed
210 during our LED test. This offset will be corrected before the retrieval. It is necessary to gate the high altitude
211 channel off for approximately the first 15 μs to maintain the PMT's linearity and minimize the impact of
212 signal-induced bias (SIB) on the background count rate. The signal from the output of the PMT is processed
213 by a 300 MHz discriminator to minimize noise counts and stored in one of four multichannel scalar (MCS)
214 boards (Tennelec/nucleus MCS-II) – one board for each channel (285High, 285Low, 291High and
215 291Low). Data files are stored in a small microcomputer and processed immediately after acquisition
216 ceases.

217 **3. Data processing**

218 3.1 Raw data processing

219 Before ozone can be retrieved, several operations, designed to improve the measurement precision, are
220 carried out. First, multiple laser shots are averaged to increase the signal-to-noise ratio (SNR). The RAPCD
221 DIAL currently uses data acquired over a 30-minute interval for each retrieval. The second step involves
222 accounting for dead time. At high counting rates (~10 MHz for the RAPCD lidar), a second signal pulse
223 arriving at the discriminator before it has recovered from the previous pulse may not be counted – a period
224 know as dead time. This time has been experimentally determined to be ~9 ns for the RAPCD lidar using

calibrated neutral density filters to characterize the system's response to accurately known count rates. A simple relationship, Eq. (1)., between the actual and measured count rates allows the impact of dead time on the data to be removed. Eq. (1). can be solved numerically for the actual count rate, r, using the measured count rate, R and the experimentally determined dead-time T_d.

$$R = re^{-rT_d} \tag{1}$$

Third, background counts due to PMT dark counts and the sky background are removed. These counts are constant and are derived using data bins for which there are no signal returns. The averaged value is then subtracted off all data channels. The final step involves smoothing the counts to reduce random noise. Our configuration currently employs a 5-point (750 m) moving average that is applied to returns from all altitudes; smoothing reduces the effectively vertical resolution to 750 m. After initial processing, a correction is applied to remove SIB from the data. This bias, also called signal-induced noise (SIN), appears as a slowly decaying, weak, noise source superimposed on the normal returns and becomes an issue if the PMT is exposed to an extremely intense light pulse (*48*). SIB can persist for several hundred microseconds and has a strong impact on data from the lidar's upper range where signal and noise counts become comparable. With uncorrected SIB, the raw signal fall off more slowly at higher altitudes resulting in lower retrieved ozone values. It is system specific and characterized under various operational conditions. For RAPCD, SIB has more influence on the shorter wavelength channel which falls off more rapidly with altitude. Unless a mechanical shutter is employed to physically block the optical path to the PMT and thereby eliminate SIB, its behavior must be characterized using a model. Cairo and Zhao have successfully used a double exponential function for this purpose (*48, 49*). However, this correction increases measurement uncertainties because both the scaling and exponential lifetimes are difficult to determine without additional independent measurements. A more practical technique is to employ a single exponential fit to the residual background (*25, 26, 50*). For the high altitude channels of the RAPCD lidar, the function's coefficients are empirically determined using a single exponential fit to data acquired ~110 to ~160 μs after data acquisition starts. The start and length of the exponential fit could vary with different

channels (either wavelength channels or altitude channels), atmospheric structures, and lidar configurations because these parameters impact the intensity of the detected signal. Future improvement to the RAPCD DIAL includes an optical chopper to remove the SIB and all need for SIB correction.

3.2 Dial retrieval

The DIAL retrieval algorithm takes advantage of the reduction of uncertainty resulting from aerosols and non-ozone absorption gases using the differential technique. The retrieval using a single wavelength becomes unreliable when aerosols and non-ozone absorption gases are present; however, conditions often exist where both single wavelength and DIAL retrievals produce comparable results. Excellent discussions concerning the DIAL technique can be found in the book by Measures [1984] and papers by Browell [1985] and Godin [1999]; a brief discussion of the technique is also provided in Appendix I.

Vertical ozone profiles can also be retrieved using a single wavelength retrieval (*51*). When sonde density profiles are available, this technique serves as an independent check on the DIAL retrievals and can provide useful information about the impact of aerosols on the measurement.

4. Performance

4.1 Raw data performance

Figure 9 (a) and (c) displays a daytime example of raw photon counts with deadtime and background corrections along with a comparison to counts expected from a model calculation. The lidar data were taken at 13:22 local time, Sep. 16, 2006, and the balloon ozonesonde measurement with a 100-m resolution was made at 13:16 the same day. A ±10% uncertainty in the ozonesonde measurement is represented by gray envelope. The ozonesonde also provides the atmospheric profiles for single wavelength retrieval, the temperature correction for ozone absorption cross section and Rayleigh correction in Dial retrieval. The raw lidar data are integrated over 36000 shots (30 min). The background including the sky light and dark counts is estimated about 1.4×10^{-2} counts/us/shot at far range for either wavelength. The PMT is gated at 3 km (20 μs). The peak counts at ~3km of both 285 and 291 are ~2.8 photons/us/shot, which gives the peak

signal-to-background ratio about 200. The signal-to-background ratio of either 285 or 291 at 10 km is less than the model calculation in Fig. 5 in part due to high ozone concentration in the lower troposphere. Though a higher signal-to-background ratio is desired, increasing the signal strength (e.g., by increasing the output energy or removing ND) will further distort the far range signal by SIB. The dead-time correction, background subtraction, moving averaging, and SIB correction are applied on the raw data as described in previous section. The final ozone profile is smoothed using a running average over 750m range cell. The averaging upon raw data and retrieved ozone profile reduce the vertical range resolution to 750m from original 150m bin width.

4.2 Retrieved ozone profile

In Fig. 9 (b) and (d) the corrected data shows good agreement with the model between 4 and 10 km. Notice some intermittent thin clouds between 11 and 12 km. Although the 291nm laser penetrates the small cloud, too few of the 285 photons survive the cloud to retrieve a useful signal. In Fig. 9 (e), the 30-min lidar retrievals agree with sonde within an accuracy of 20% at all altitudes. The error bars show the 1-sigma statistical uncertainty of the DIAL retrieval over a 30-min interval. The error bars indicate that the DIAL measurement precision increases from 5% at 4 km to ~50% at 10 km. Fig. 9(e) indicates good consistency between the single wavelength retrievals at both wavelengths and the DIAL retrieval between 4 and 10 km.

5. Error Analysis

According to the sources, we can divide the errors in DIAL measurements into four categories: 1). Statistical uncertainties, ε_1 ,due to atmospheric turbulence effects, signal, and background noise fluctuations; 2). Error, ε_2 , due to differential backscattering and extinction of non-ozone gases (O_2, SO_2, NO_2, etc.) and aerosols; 3). Error, ε_3 , due to ozone absorption cross section; and 4). Error, ε_4 , related to instruments and electronics. ε_1 is a random error; ε_2 , ε_2 , and ε_3 are systematical errors.

5.1 Statistical error

297 With the assumption of a Poisson distribution governing photon counting, ε_1 can be written as:

298 $$\varepsilon_1 = \frac{1}{2O_3(R+1/2\Delta R)\Delta R\Delta\sigma_{O3}}\sqrt{\frac{1}{P_{on}(R)}+\frac{1}{P_{on}(R+\Delta R)}+\frac{1}{P_{off}(R)}+\frac{1}{P_{off}(R+\Delta R)}} \quad (2)$$

299 It is easy to show that ε_1 is proportional to $(\Delta R^3 NAP_L)^{-1/2}$, where N is the shots of integration and A is the
300 area of the telescope and P_L is the emitted laser power. ε_1 also depends on the weather condition and
301 vertical ozone structure. For 750 m vertical resolution and 36000-shot integration, generally ε_1 is <5% at
302 4 km and 40%-60% at 10 km in our DIAL retrievals.

303 5.2 Interference by non-ozone species

304 ε_2 includes the interference from O_2, SO_2, NO_2, and aerosols. The O_2 interference should be
305 considered as one of the error sources in the DIAL retrieval (*52*) because the quantity of O_2 is large in the
306 atmosphere. The O_2 absorption spectrum below 300 nm is composed of the Herzberg band system and the
307 O_2-O_2 and O_2-X collision-induced absorption bands (*53*). The accurate calculation of the O_2 interference is
308 difficult because the oxygen dimmer absorption theory has not been entirely established (*54*), and the
309 uncertainty of the O_2 cross section measurement is quite high. Based on the data set of the Fally group (*53,*
310 *55, 56*), the differential O_2 effective absorption cross section (*57*) is less than 4.5×10^{-27}, which results a
311 DIAL retrieval error <1.5% with a 60ppbv ozone mixing ratio. As discussed in a previous section, the
312 errors due to SO_2 are ~-0.01% under clear conditions and ~-0.1% under very polluted conditions. The NO_2
313 absorption cross sections at 285 and 291 are 7.07×10^{-20} and 9.32×10^{-20} cm^2 respectively at 293K with an
314 uncertainty of 3.2% (*58*). The NO_2 differential cross section is -2.25×10^{-20} cm^2 for the 285 and 291 pair.
315 NO_2 is highly variable and inhomogeneous over time and space. The mean NO_2 mixing ratios over Houston
316 and Nashville are recorded less than 0.2 ppbv above 800 hPa in the Texas Air Quality Study (TexAQS) and
317 Southern Oxidants Study (SOS) (*59*), leading to the DIAL retrieval error ~-0.007% under the 60ppbv
318 constant ozone assumption. The HCHO absorption cross sections at 285 and 291 are 4.17×10^{-20} and
319 2.06×10^{-20} cm^2, respectively, at 293K (*58*) result in an HCHO differential cross section of 2.11×10^{-20} cm^2.

The local HCHO information is not available. The maximum HCHO mixing ratio at 600 hpa (~4.3 km) recorded in Houston was 150 pptv during TexAQS and SOS campaign (*59*). This leads to a 0.015% error in DIAL retrieval. The impact caused by differential Rayleigh extinction can be modeled within an accuracy of 1% using balloon sonde retrievals of atmospheric density or by employing climatological models.

The main concern comes from the aerosol interference which depends on the wavelengths and wavelength separation. Even though the aerosol optical properties could be retrieved from a third wavelength, the differential effect for a DIAL wavelength pair still has some uncertainty. Within the PBL, where the statistical errors are small, differential aerosol backscattering and extinction can be the dominant error sources for a DIAL ozone retrieval (*22, 24, 25*). Our model simulation in Fig. 6(b) has shown the DIAL retrieval errors due to aerosol could be up to 25% in PBL when aerosol loading is 10 times higher than the average. In the free-troposphere, the aerosol concentration decreases very quickly and the increasing statistical errors quickly dominate. The errors due to aerosols are smaller than 1% above 4 km using fall-winter rural aerosol model. If the aerosol values are increased by a factor of ten, the resulting ozone uncertainties increase to 5% at 4 km.

5.3 Uncertainty in ozone absorption cross section

ε_3 The uncertainty of Bass-Paur ozone cross section is believed to be less than 2% (*54, 60, 61*). The retrieval error due to ozone absorption cross section should be less than 3% even with the temperature dependence considered.

5.4 Errors related to instruments and electronics

ε_4 could be caused by misalignment, imperfect dead-time, and SIB correction. The first aspect is negligible when both lasers are well-aligned and reach the full overlap altitude. The latter two can be investigated by an LED or null-profile test. The error caused by SIB usually is larger than dead-time since the dead-time behavior can be easier characterized. The SIB can be estimated better by exponential fit with longer integration. For the 36000-shot integration data, ε_4 is believed to be <1% at 4 km and <5% at 8 km.

344 The summary of the errors in RAPCD-DIAL measurement is given by Table 3 assuming 60 ppbv constant
345 ozone in troposphere for a 36000-shot integration data.
346 An example of continuous lidar measurements is shown by Fig. 10. Ten 30-minute DIAL
347 measurements shown in Fig. 10 (a) were made between 11:00 and 17:00 local time on Dec. 23, 2006. Fig.
348 10 (b) shows the average Dial profile of the 10 retrievals and its 1-sigma standard deviation which
349 represents the measured uncertainty. The average ozone DIAL profile shows good agreement with
350 ozonesonde measurement between 4 and 10km. The standard deviation increases from ~5% at 4 km to
351 ~60% at 10 km. This data set along with the ozonesonde measurements show that ε_1 is most significant in
352 all of the errors though the ozone variation could contribute a small part to the different between the DIAL
353 and ozonesonde.

354 **6. Future work**

355 6.1 Modifications to the high altitude channel

356 The effectiveness of the current system's high-altitude channels is limited by the need to electronically
357 protect against the large backscattering signal originating from the first kilometer or so above the telescope.
358 These large initial signals interfere with the PMT's linearity and make it difficult to properly characterize
359 the PMT's background count rate. The current system attempts to minimize these effects through a
360 combination of several techniques. The first technique restricts the backscattered signal by limiting the
361 maximum per pulse laser energy and by attenuating the signal before reaching the high channel through a
362 combination of optical splitters and neutral density filters. Both approaches reduce signal returns from
363 higher altitudes thereby limiting the maximum achievable altitude and/or increasing signal averaging time.
364 An electronic gating circuit is employed that permits the gain of the PMT to be turned off for periods as
365 short as 10 microseconds. Although this does not protect the photocathode directly, it does prevent the
366 resulting photoelectrons from being amplified and causing both gain and background nonlinearity problems
367 in the future. This technique, however, provides only partial protection from the problems caused by the
368 large initial backscatter pulses. The final approach raises the altitude at which complete overlap between

the laser beam and telescope's FOV occurs. This technique reduces the initial backscatter pulse as seen by the detector but occurs at the cost of signal from the lower end of the channel's range. We intend to resolve these issues through the addition of a mechanical chopper. Choppers are routinely employed on lidar systems to protect PMTs by physically blocking the optical path between the telescope and PMT. This blocking prevents the large initial backscatter pulse from being seen by the PMT's photocathode. Shielding the high channel's PMT from returns originating within the first couple of kilometers will permit higher, per pulse, laser energies thus enabling faster data acquisition, higher maximum altitudes, and higher measurement precision.

6.2 Modifications to the low-altitude channel

The current low-altitude channel is ineffective because the separation between laser beam and the telescope (optimized for the high altitude channel) is too great for full overlap in the PBL. The integrated modification will introduce a primary mirror with an effective diameter of 10 cm rather the 40 cm. The smaller telescope will thus collect fewer photons from an altitude range that already sees extremely large signals and will experience complete overlap at a much lower altitude than is currently the case. The current PMTs, EMI 9813s, will be replaced by the much smaller Hamamatsu 7400s; this change will significantly shrink the size of the instrument with no sacrifice to performance. These PMTs have already seen extensive operational use on the NASA GSFC AROTEL lidar. Three separate splitters will allow a custom determination of the optimum signal split between these channels. The detection electronics for the high and low channels will be updated by replacing the current multi-channel scalar boards with state-of-the-art detection modules having both simultaneous analog and photon counting capabilities.

To enhance the lidar's measurement capabilities within the boundary layer, a scanner will be added to permit range resolved measurements of ozone from the surface to the top of the PBL in any direction. This consideration will enable the study of pollution transport within the PBL at high resolution and permit the study of ozone variability on spatial scales of hundreds of meters.

7. Conclusion

394 The RAPCD-DIAL system can measure ozone profiles between 4 and 10 km with an errors ranging from
395 <8% at 4k m to 40%~60% at 10 km. The error sources include the statistical uncertainty, differential
396 scattering and absorption from non-ozone species, uncertainty in ozone absorption cross section, and
397 imperfection of dead-time and SIB correction. The statistical uncertainty dominates the error sources and
398 could be reduced by increasing the sampling time or reducing the range resolution. The aerosol interference
399 in the free-troposphere is relatively small. A mechanical chopper will be added into our high-altitude
400 channel to improve signal linearity. A smaller telescope and detection modules will be used for our
401 low-altitude channel in the future to decrease the full overlap altitude and avoid PMT saturation in the near
402 range.

403 **8. Acknowledgements**

404 We gratefully acknowledge the assistance of Tom McGee/GSFC and Stuart McDermid/JPL in the design
405 and construction of the RAPCD DIAL tropospheric ozone system. NASA Earth Science Program provided
406 support. We thank Ms. Whitney Guerin for her kind help in editing the manuscript. This research was
407 performed as part of Shi Kuang's Ph.D. degree requirements and he would like to thank his advisor,
408 Michael J. Newchurch, for his support and encouragement.

409

410 **Appendix**

411 **A. Dial retrieval algorithm**

412 The average ozone number density above full overlap altitude between range R and $R+\Delta R$ is solved by:

413 $$[O_3](R+\frac{1}{2}\Delta R)=$$

414 $$\frac{1}{2\Delta R\Delta\sigma_{O3}}\ln[\frac{P_{on}(R)P_{off}(R+\Delta R)}{P_{off}(R)P_{on}(R+\Delta R)}] \quad \text{(A1a)}$$

415 $$-\frac{1}{2\Delta R\Delta\sigma_{O3}}\ln[\frac{\beta_{off}(R)\beta_{on}(R+\Delta R)}{\beta_{on}(R)\beta_{off}(R+\Delta R)}] \quad \text{(A1b)}$$

416 $$-\frac{1}{\Delta\sigma_{O3}}(\alpha_{on}-\alpha_{off}) \quad \text{(A1c)}$$

417 where the subscript 'on' and 'off' represent the on-line and off-line wavelengths respectively; P is
418 detected power or photons; β is total backscatter coefficient; α is total extinction coefficient except for
419 ozone absorption; $\Delta\sigma_{O3}$ is differential ozone absorption cross section. P, β, and α are dependents of
420 R and wavelength. Strictly, $\Delta\sigma_{O3}$ is R dependent, as well, because it is the function of temperature which
421 varies with R. The DIAL equation reduces to only (A1a), signal term when the differential scattering and
422 extinction from non-ozone species are ignored. Term (A1b), differential backscattering term, consists of
423 Rayleigh (molecular) and Mie (aerosol) differential backscattering. Term (A1c), differential extinction term,
424 consists of differential Rayleigh extinction, aerosol extinction, and non-ozone gaseous absorption including
425 O_2, SO_2, NO_2 etc. Rayleigh effects usually can be corrected in practice with the assistance of a local
426 atmospheric sonding profile. The aerosol effects should be corrected when they are significant enough,
427 especially in PBL.

428 **B. Single wavelength retrieval algorithm**

429 The vertical ozone profile can be retrieved using the backscattered signal of one laser with the Rayleigh and

Mie backscattering and extinction known. The average ozone number density between R and $R+\Delta R$ is solved by (*62*):

$$[O_3](R+\frac{1}{2}\Delta R)=\frac{1}{2\sigma_{O3}\Delta R}\times\{\ln[\frac{P_\lambda(R)}{P_\lambda(R+\Delta R)}]-\ln[\frac{\beta_\lambda(R)/R^2}{\beta_\lambda(R+\Delta R)/(R+\Delta R)^2}]-2\alpha_\lambda(R)\Delta R\} \quad \text{(B1)}$$

Where λ is wavelength and σ_{O3} is absorption cross section of ozone. $\beta_\lambda(R)$ is the sum of Rayleigh and Mie components. $\alpha_\lambda(R)$ is the sum of Rayleigh, Mie, and absorption gaseous components. $\beta_\lambda(R)$ and $\alpha_\lambda(R)$ can be approximately reduced to only Rayleigh component in the unpolluted free-troposphere and stratosphere. However, the retrieval with a single laser tends to be unreliable when aerosols and other non-ozone absorption gases are heavily present. The single wavelength retrieval is also more sensitive to the atmospheric density profile than DIAL retrieval. The errors of single wavelength retrieval are discussed in another paper. Interested readers should refer to Measures' book. However, when simultaneous atmospheric temperature and pressure profiles are available, it will be a good reference for our DIAL retrieval in the free-troposphere where aerosols are much less of a concern than in the PBL.

443

444 **REFERENCES**

445

446 1. A. J. DeCaria, K. E. Pickering, G. L. Stenchikov, L. E. Ott, "Lightning-generated NOX and its
447 impact on tropospheric ozone production: A three-dimensional modeling study of a
448 Stratosphere-Troposphere Experiment: Radiation, Aerosols and Ozone (STERAO-A)
449 thunderstorm" *J. Geophys. Res.* **110** (2005).
450 2. J. Lelieveld, F. J. Dentener, "What controls tropospheric ozone?" *J. Geophys. Res.* **105**, 3531
451 (2000).
452 3. S. J. Oltmans *et al.*, "Summer and spring ozone profiles over the North Atlantic from ozonesonde
453 measurements" *J. Geophys. Res.* **101**, 29 (1996).
454 4. M. J. Newchurch, D. Sun, J. H. Kim, X. Liu, "Tropical Tropospheric Ozone Derived using
455 Clear-Cloudy Pairs (CCP) of TOMS Measurements" *J. of Atmos. Chem. Phys.* **3**, 683 (2003).
456 5. R. D. McPeters *et al.*, *Nimbus-7 Total Ozone Mapping Spectrometer (TOMS) Data Products User's*
457 *Guide*, NASA (Washington, D.C., 1996).
458 6. M. P. McCormick, J. M. Zawodny, R. E. Veiga, J. C. Larsen, P. H. Wang, "An overview of SAGE
459 I and II ozone measurements" *Planet Space Sci.* **37**, 1567 (1989).
460 7. D. M. Cunnold, L. Froidevaux, J. M. Russell, B. Connor, A. Roche, "Overview of UARS ozone
461 validation based primarily on intercomparisons among UARS and Stratospheric Aerosol and Gas
462 Experiment II measurements" *J. Geophys. Res.* **101**, 10 (1996).
463 8. J. M. Russell III *et al.*, "The Halogen Occultation Experiment" *J. Geophys. Res.* **98**, 10 (1993).
464 9. M. J. Newchurch, D. M. Cunnold, H. J. Wang, "Stratospheric Aerosol and Gas Experiment
465 II--Umkehr ozone profile comparisons" *J. Geophys. Res.* **100**, 14029 (1995).
466 10. M. J. Newchurch, D. M. Cunnold, J. Cao, "Intercomparison of Stratospheric Aerosol and Gas
467 Experiment (SAGE) with Umkehr[64] and Umkehr[92] ozone profiles and time series: 1979-1991"
468 *J. Geophys. Res.* **103**, 31 (1998).
469 11. J. P. Burrows *et al.*, "The Global Ozone Monitoring Experiment (GOME): Mission concept and
470 first scientific results" *J. Atmos. Sciences* **56**, 151 (1999).
471 12. R. D. McPeters, G. J. Labow, B. J. Johnson, "A satellite-derived ozone climatology for
472 balloonsonde estimation of total column ozone" *J. Geophys. Res.* **102**, 8875 (1997).
473 13. K. V. Chance, J. P. Burrows, D. Perner, W. Schneider, "Satellite measurments of atmospheric
474 ozone profiles, including tropospheric ozone, from ultraviolet/visible measurements in the nadir
475 geometry: a potential method to retrieve tropospheric ozone" *J. Quant. Spectrosc. Radiat. Transfer*
476 **57**, 467 (1997).
477 14. J. R. Ziemke, S. Chandra, P. K. Bhartia, "Two new methods for deriving tropospheric column
478 ozone from TOMS measurements: Assimilated UARS MLS/HALOE and convective-cloud
479 differential techniques" *J. Geophys. Res.* **103**, 22 (1998).
480 15. J. H. Kim, M. J. Newchurch, K. Han, "Distribution of Tropical Tropospheric Ozone determined by
481 the scan-angle method applied to TOMS measurements" *J. Atmos. Sci.* **58**, 2699 (2001).
482 16. J. H. Kim, S. Na, M. J. Newchurch, K.J. Ha, "Comparison of Scan-Angle Method and Convective
483 Cloud Differential Method in Retrieving Tropospheric Ozone from TOMS" *Environ. Mon. Assess.*
484 **92**, 25 (2004).
485 17. J. H. Kim, M. J. Newchurch, "Climatology and trends of tropospheric ozone over the eastern
486 Pacific Ocean: The influences of biomass burning and tropospheric dynamics" *Geophys. Res. Lett.*
487 **23**, 3723 (1996).
488 18. X. Liu *et al.*, "Ozone profile and tropospheric ozone retrievals from Global Ozone Monitoring
489 Experiment: Algorithm description and validation" *J. Geophys. Res.* **110** (2005).

19. M. J. Newchurch, X. Liu, J. H. Kim, P. K. Bhartia, "On the accuracy of TOMS retrievals over cloudy regions" *J. Geophys. Res.* **106**, 32 (2001).
20. M. J. Newchurch, X. Liu, J. H. Kim, "Occurrence of Ozone Anomalies over Cloudy Areas in TOMS Version-7 Level-2 Data" *J. Geophys. Res.* (2000).
21. Y. Zhao, R. D. Marchbanks, R. M. Hardesty, paper presented at the 42nd SPIE Annual meeting, Application of Lidar to Current Atmospheric Topics II, Proceedings of SPIE #3127 1997.
22. E. V. Browell, S. Ismail, S. T. Shipley, "Ultraviolet DIAL measurements of O3 profiles in regions of spatially inhomogeneous aerosols" *App. Opt.* **24**, 2827 (1985).
23. G. Ancellet, A. Papayannis, J. Pelon, G. Mégie, "DIAL Tropospheric Ozone Measurement Using a Nd:YAG Laser and the Raman Shifting Technique" *J. of Atmos. Ocean. Tech.* **6**, 832 (1989).
24. A. Papayannis, G. Ancellet, J. Pelon, G. Mègie, "Multiwavelength lidar for ozone measurements in the troposphere and the lower stratosphere" *App. Opt.* **29**, 467 (1990).
25. J. A. Sunesson, A. Apituley, D.P.J.Swart, "Differential absorption lidar system for routine monitoring of tropospheric ozone" *App. Opt.* **33**, 7045 (1994).
26. M. H. Proffitt, A. O. Langford, "Ground-based differential absorption lidar system for day or night measurements of ozone throughout the free-troposphere" *App. Opt.* **36**, 2568 (1997).
27. T. Fukuchi, "Tropospheric O3 measurements by simultaneous differential absorption lidar and null profiling" *Opt. Eng.* **40** (2001).
28. J. Pelon, S. Godin, G. Megie, "Upper stratospheric (30-50 km) lidar observations of the ozone vertical distribution" *J. Geophys. Res.* **91**, 8667 (1986).
29. O. Uchino, I. Tabata, "Mobile lidar for simultaneous measurements of ozone, aerosols, and temperature in the stratosphere" *App. Opt.* **30**, 2005 (1991).
30. T. J. McGee, M. R. Gross, U. N. Singh, J. J. Butler, P. E. Kimvilakani, "Improved stratospheric ozone lidar" *Opt. Eng.* **34**, 1421 (1995).
31. I. S. McDermid, "Differential absorption lidar system for tropospheric and stratospheric ozone measurements" *Opt. Eng.* **30** (1991).
32. E. V. Browell, S. Ismail, W. B. Grant, "Differential absorption lidar(DIAL) measurements from air and space" *App. Phys.*, 399 (1998).
33. E. V. Browell *et al.*, "NASA multipurpose airborne DIAL system and measurements of ozone and aerosol profiles" *App. Opt.* **22**, 522 (1983).
34. T. J. McGee *et al.*, "The Airborne, Raman Ozone, Temperature and Aerosol Lidar (AROTAL): Instrument and Measurements" *in prep.* (2007).
35. S. McDermid, G. Beyerle, D. A. Haner, T. Leblanc, "Redesign and improved performance of the tropospheric ozone lidar at the Jet Propulsion Laboratory Table Mountain Facility" *App. Opt.* **41**, 7550 (2002).
36. U. Kempfer, W. Carnuth, R. Lotz, T. Trickl, "A weide-range ultraviolet lidar system for tropospheric ozone measurements: Development and application" *Rev. Sci. Instrum.* **65**, 3145 (1994).
37. O. R. Cooper *et al.*, "A springtime comparison of tropospheric ozone and transport pathways on the east and west coasts of the United States" *J. Geophys. Res.* **110**, 21 (2005).
38. G. J. Megie, G. Ancellet, J. Pelon, "Lidar measurements of ozone vertical profiles" *Appl. Opt.* **24** (1985).
39. M. J. Newchurch, M. A. Ayoub, S. Oltmans, B. Johnson, F. J. Schmidlin, "Vertical Distribution of Ozone at Four Sites in the United States" *J. Geophys. Res.* **108(D1)**, 4031 (2003).
40. A. S. Jursa, "Handbook of Geophysics and the Space Environment" (1985).
41. T. F. Eck *et al.*, "Wavelength dependence of the optical depth of biomass burning, urban, and desert dust aerosols" *J. Geophys. Res.* **104**, 31 (1999).
42. A. G. Wright, "An Investigation of Photomultiplier Background" *J. Phys. E: Sci. Instrum.* **16**, 300 (1983).
43. S. Madronich, S. Flocke, paper presented at the NATO ASI Series I: Global Environmental Chang,

Berlin 1997.
44. J. Rufus, G. Stark, P. L. Smith, J. C. Pickering, A. P. Thorne, "High-resolution photoabsorption cross section measurements of SO2, 2: 220 to 325 nm at 295 K" *J. Geophys. Res.* **108** (2003).
45. J. H. Seinfeld, S. N. Pandis, *Atmospheric Chemistry and Physics, From Air Pollution to Climate Change*, John Wiley & Sons (New York, 1998).
46. ISO, *Standard for the Measurement of Beam Widths, Beam Divergence, and Propagation Factors, Proposal for a Working Draft* (1991).
47. S. Kuang, J. Burris, M. J. Newchurch, S. Johnson, "Diagnosis of Lidar systematic errors by LED synthetic signal" *in prep* (2007).
48. F. Cairo, F. Congeduti, M. Poli, S. Centurioni, G. d. Donfrancesco, "A survey of the signal-induced noise in photomultiplier detection of wide dynamics luminous signals" *Rev. Sci. Instrum.* **67**, 3274 (1996).
49. Y. Zhao, "Signal-induced fluorescence in photomultipliers in differential absorption lidar systems" *Appl. Opt.*, **38** (1999).
50. T. J. McGee *et al.*, "Lidar measurements of stratospheric ozone during the STOIC campaign" *J. Geophys. Res.* **100**, 9255 (1995).
51. O. Uchino, M. Maeda, M. Hirono, "Applications of Excimer lasers to Laser-Radar Observations of the Upper Atmosphere" *IEEE J. Quantum Electron.* **QE-15** (1979).
52. R. Volkamer, T. Etzkorn, A. Geyer, U. Platt, "Correction of the oxygen interference with UV spectroscopic (DOAS) measurements of monocyclic aromatic hydrocarbons in the atmosphere" *Atmos. Enviro.* **32**, 3731 (1998).
53. S. Fally *et al.*, "Fourier Transform Spectroscopy of the 02 Herzberg bands. III. Absorption cross-sections of the collision-induced bands and of the Herzberg continuum" *J. Mol. Spectrosc.* **204**, 10 (2000).
54. J. Orphal, "A critical review of the absorption cross-sections of O3 and NO2 in the 240-790 nm region" *J. Phtotoch. and Photobio. A.*, 185 (2003).
55. A. Jenouvrier *et al.*, "Fourier transform spectroscopy in the O2 Herzberg bands: I- Rotational analysis" *J. Mol. Spectrosc.* **198**, 136 (1999).
56. M.-F. Mérienne *et al.*, "Fourier transform spectroscopy of the O2 Herzberg bands. II. Band oscillator strengths and transition moments" *J. Mol. Spectrosc.* **202**, 171 (2000).
57. A. Amoruso, L. Crescentini, "Oxygen dimerization and pressure dependence of the absorption cross-section in the Herzberg continuum" *J. Quant. Spect. Rad. Trans.* **53**, 457 (1995).
58. K. Bogumil *et al.*, "Measurements of molecular absorption spectra with the SCIAMACHY pre-flight model: instrument characterization and reference data for atmospheric remote-sensing in the 230–2380 nm region" *J. Photochem. Photobiol A: Chem* **157**, 167 (2003).
59. R. V. Martin *et al.*, "Evaluation of GOME satellite measurements of tropospheric NO 2 and HCHO using regional data from aircraft campaigns in the southeastern United States" *J. Geophys. Res.* **109** (2004).
60. A. M. Bass, R. J. Paur, "Absorption cross-sections for ozone: the temperature dependence" *J. Photochem.* **17** (1981).
61. J. Orphal, K. Chance, "Ultraviolet and visible absorption cross-sections for HITRAN" *J. Quant. Spectrosc. Radiat. Trans.* **82**, 491 (2003).
62. M. R. Measures, "Laser remote sensing: Fundamentals and applications" (1984).

586

587 Table 1. Parameters for model simulation

Laser energy	4 mJ/pulse
The diameter of telescope primary mirror	40 cm
Telescope field-of-view	1.5 mrad
Receiver bandwidth	1 nm
PMT quantum efficiency	20%
Total optical transmission efficiency	5%
Solar zenith angle	30°
Temperature and Pressure profiles	1976 US standard atmosphere
Ozone profile	mean profile over Huntsville in 2005
Aerosol profile	fall-winter rural aerosol model

588

589

590

591 Table 2. Characteristics of DIAL system

System	Specification
Transmitter	
Lasers	Continuum Nd:YAG, 20 Hz repetition rate, 5-7 ns pulse length, ~300 mJ/pulse at 1064 nm, 80 mJ/pulse at 532 nm
Dye	Rhodamine 590 and 610
Emitted energy	4-5 mJ/pulse at 285 nm, divergence<1 mrad 3-4 mJ/pulse at 291 nm, divergence<1 mrad
Receiver	
Telescope	Newtonian, 40.6 cm diameter, f/4.5, 1.5 mrad FOV
Filter	Barr band-pass filter (286.4/11nm) and neutral density filters
Detector	Electron Tubes 9813QA, ~28% quantum efficiency
Discriminator	Phillips Scientific 300 MHz
Signal Processing	Tennelec/nucleus MCS-II cards, 200 MHz, 24 bit

592

593

Table 3. Summary of the errors in RAPCD-DAIL measurements*

Errors		4 km	10 km
ε_1, statistical error		~5%	~40-60%
ε_2, interference by non-ozone species	Aerosol	~1% under clear condition; ~5% under haze condition	~1%
	SO_2	~-0.01% under normal condition ~-0.1% under polluted condition	
	NO_2	~-0.007%	
	O_2	~1.5%	
	HCHO	~0.015%	
	Rayleigh	~1% using local radiosonde profile	
ε_3, due to uncertainty in $\Delta\sigma_{O3}$		~3%	
ε_4, due to SIB and dead-time		~1%	~5%
Total error		~6.3%-~8.0%	~40.5%-~60.3%

* The errors are estimated by assuming 60 ppbv constant ozone in troposphere for 750 m vertical resolution and 36000-shot integration data.

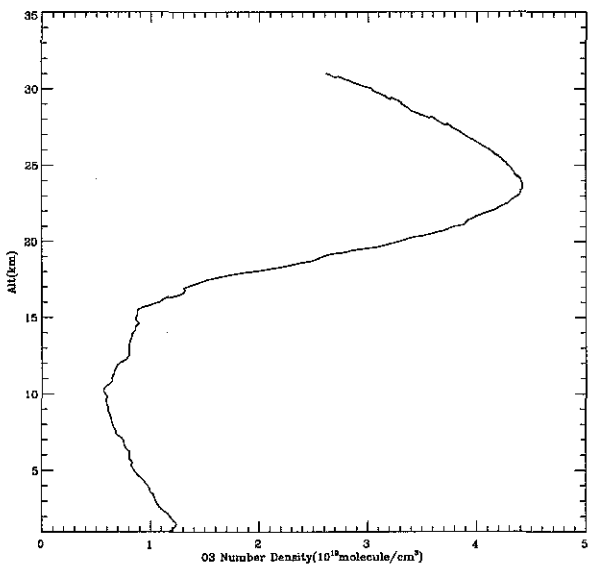

Fig. 1. Mean ozone profile over Huntsville (2005). Huntsville ozone station in UAH routinely launches balloon ozonesonde weekly at 19:00 UTC on Saturday. The ozonesondes measure ozone up to 35km with a 100 m vertical resolution and 5-10% accuracy.

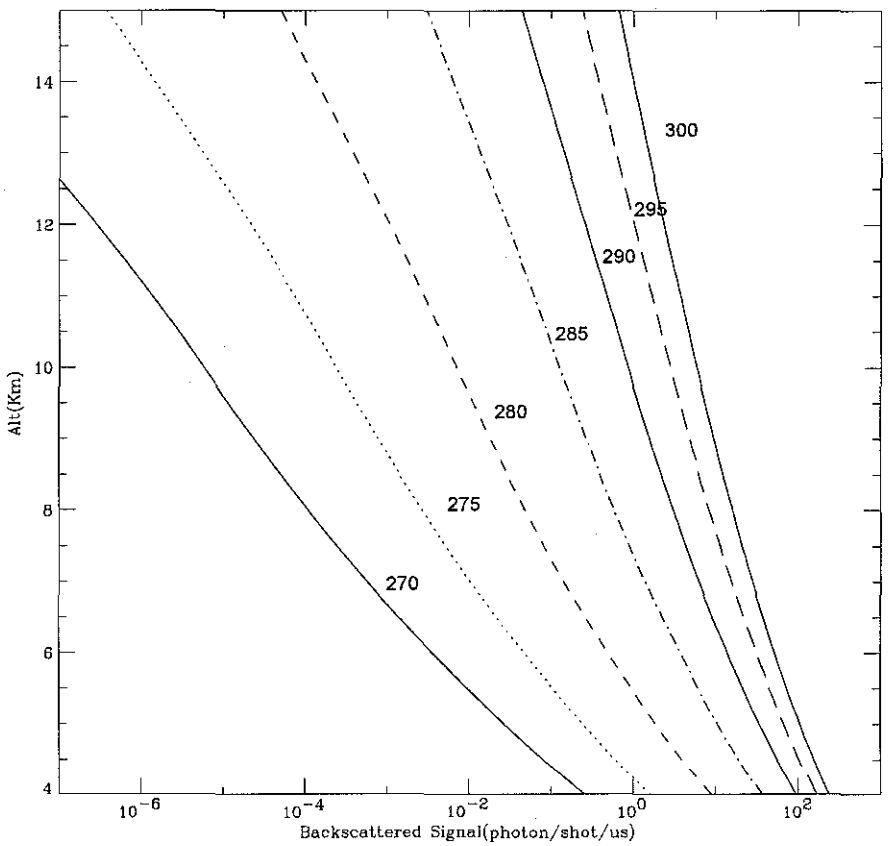

Fig. 2. Modeled lidar signal returns from 270 to 300 nm using the parameters in Table 1.

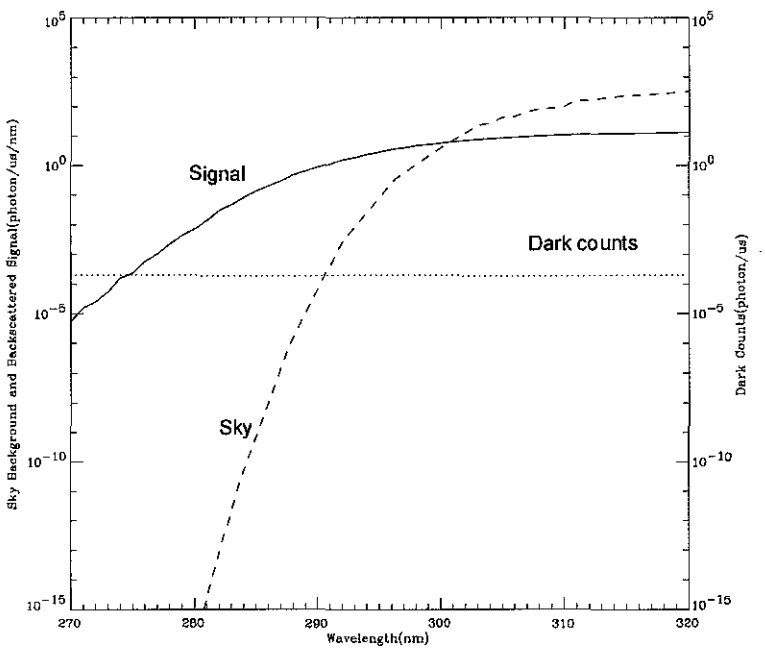

Fig. 3. Comparison of expected background including sky background and dark counts with modeled signal return at 10km without band-pass filter. The signal return and sky background are simulated with the parameters in Table 1.

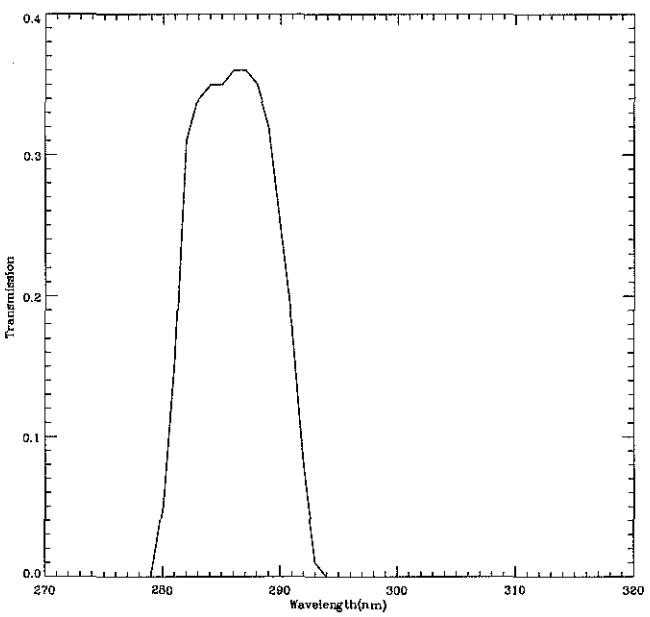

Fig. 4. Transmission of Barr filters (286.4/11nm) as a function of wavelength.

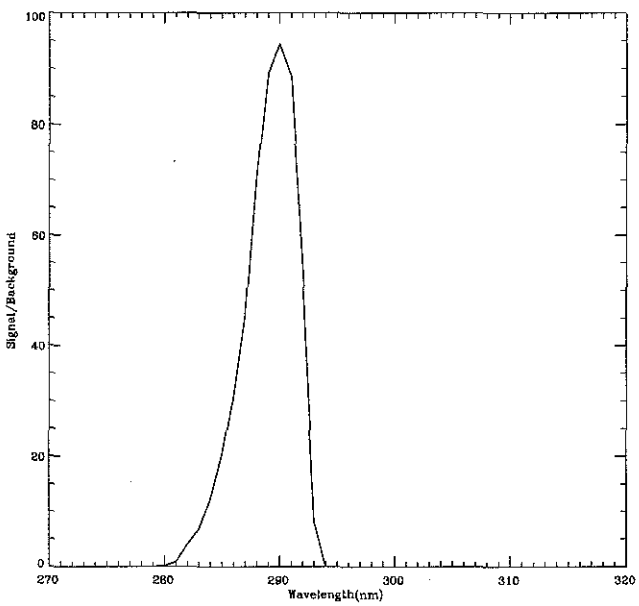

Fig. 5. Expected signal-to-background ratio at 10 km after passing through the band-pass filter as a function of wavelength. The signal return and sky background are modeled with the parameters in Table 1. The sky background is integrated over the transmission of band-pass filter in Fig. 4. The dark counts are assumed constant level at 200 photons/s.

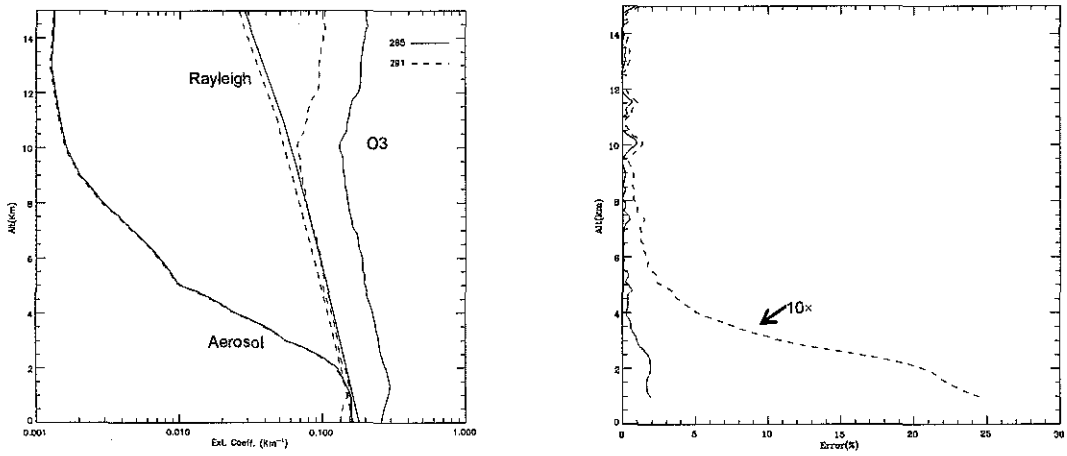

Fig. 6. Modeled DIAL retrieval errors due to aerosol. (a) Extinction as a function of altitude for aerosols (using the rural fall-winter aerosol profiles at 285 and 291 nm), Rayleigh scattering (using the 1976 US Standard Atmosphere) and ozone (using the 2005 Huntsville averaged ozone profile). (b) DIAL retrieval errors due to differential aerosol backscattering and extinction for 285-291 nm pair with a 750 m range resolution. The solid line represents the corresponding retrieval error of the aerosol model in (a). The dash line represents the retrieval error arising from an aerosol loading 10 times higher than given in the aerosol model in (a).

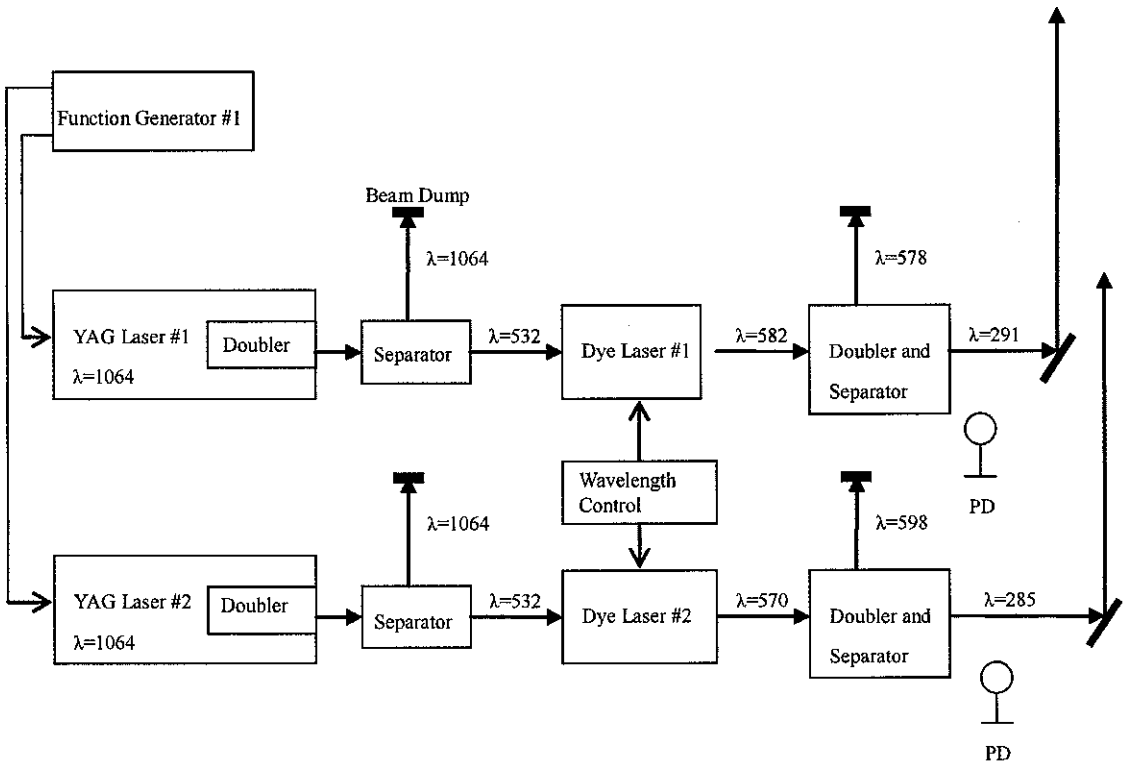

Fig. 7. Transmitter diagram.

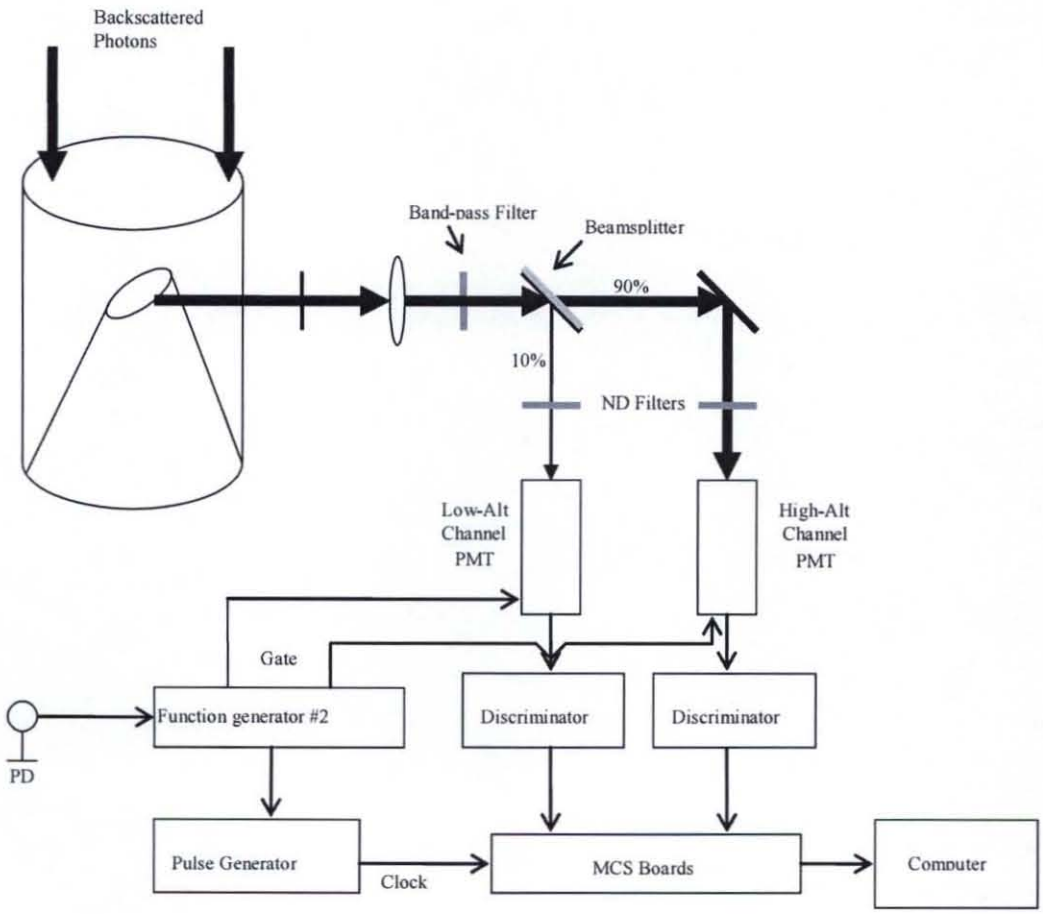

Fig. 8. Diagram of the receiver and detector.

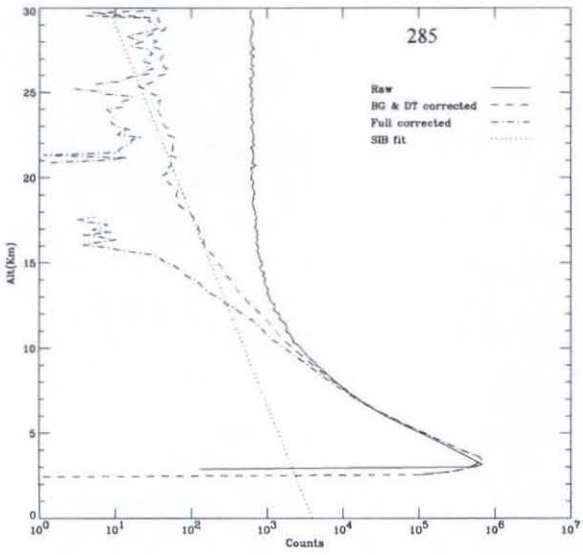
285
Raw
BG & DT corrected
Full corrected
SIB fit
Alt(Km)
Counts

(a)

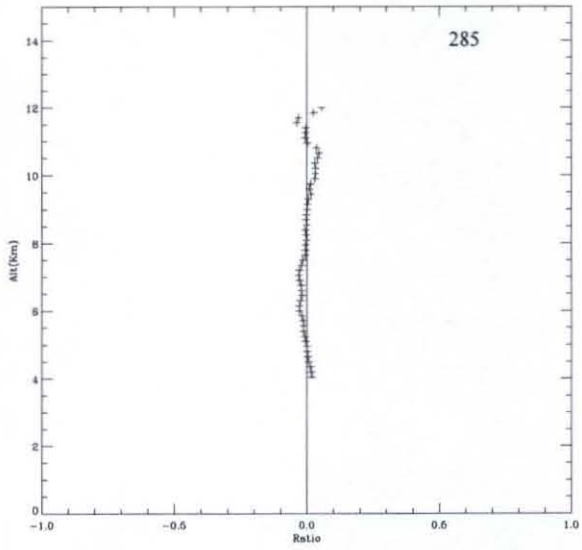
285
Alt(Km)
Ratio

(b)

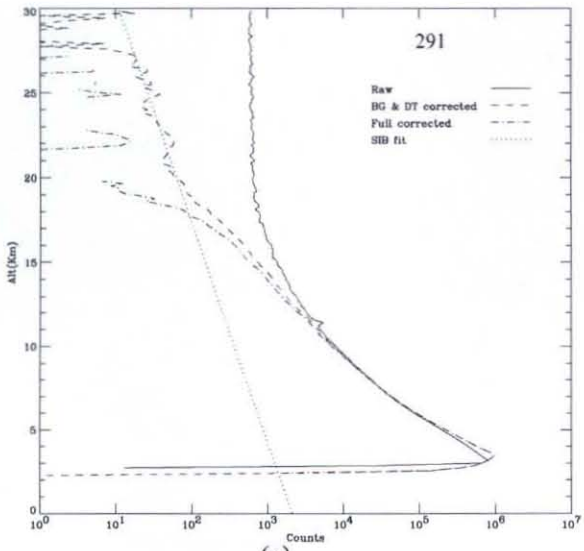
291
Raw
BG & DT corrected
Full corrected
SIB fit
Alt(Km)
Counts

(c)

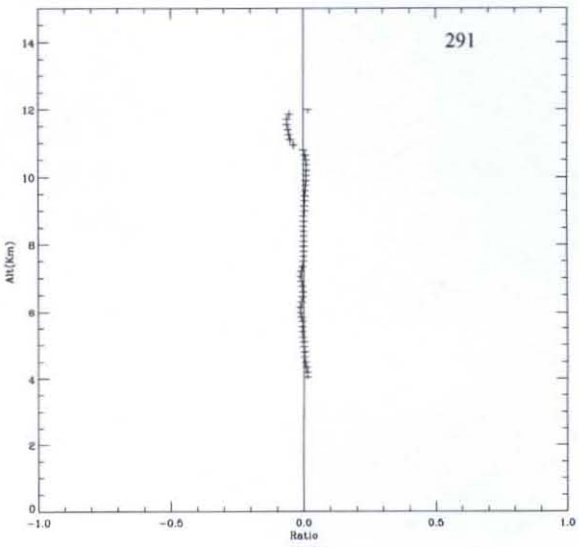
291
Alt(Km)
Ratio

(d)

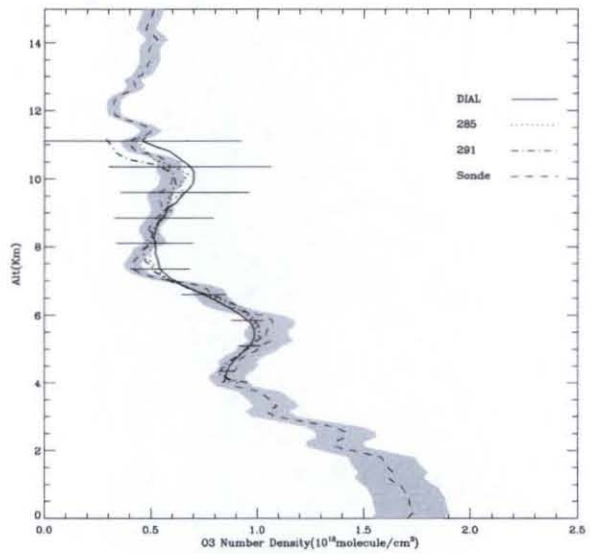

(e)

Fig. 9. DIAL daytime measurement at 13:22 local time, Sep. 16, 2006. (a) 285nm raw, background-and-dead-time (BG & DT) corrected, and fully corrected data. The raw data were integrated over 36000 shots, 30 min for 20Hz repetition frequency. (b) Difference, (model-data)/model, between 285 fully corrected data and model. (c) 291nm raw, dead-time-and-background corrected, and fully corrected data. (d) Difference, (model-data)/model, between 291 fully corrected data and model. (e) Comparison of ozonesonde measurement and DIAL and with single wavelength retrievals with 750 m vertical resolution. The balloon ozonesonde was launched at 13:16 local time and also provided the temperature and pressure profiles to calculate single wavelength retrieval, correct ozone absorption cross section and Rayleigh effects in Dial retrieval. The ±10% uncertainty of the ozonesonde is represented by gray envelope. The error bars represent the 1-sigma statistical uncertainty of Dial retrieval.

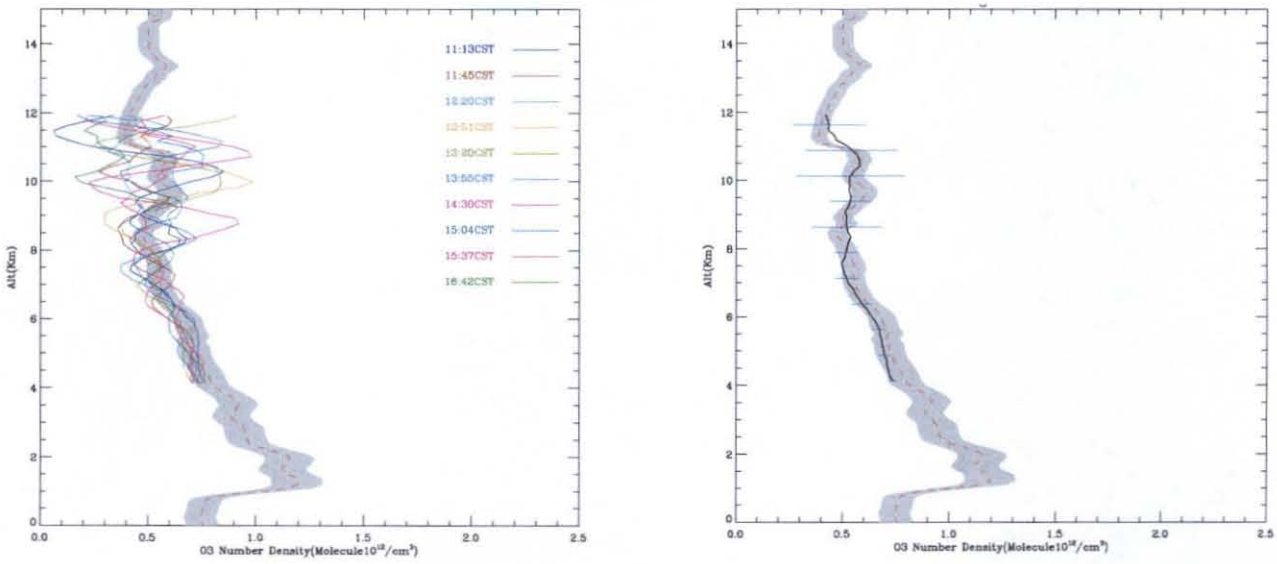

(a) (b)

Fig. 10. Continuous DIAL measurements compared with local ozonesonde measurement. (a Coincident ozone DIAL retrievals (solid lines) with 750 m vertical resolution and 30 min integration time and ozonesonde profile (dash line) with ±10% envelope on 12/23/06. The ozonesonde measurement was made at 13:00 local time. (b) Average Dial profile of the 10 retrievals shown in (a) and its 1-sigma standard deviation.